The rate of information transmission through the MAPK/ERK signaling pathway stimulated in a pulsatile manner

Paweł Nałęcz-Jawecki[1], Paolo Armando Gagliardi[2], Marek Kochańczyk[1], Coralie Dessauges[2], Olivier Pertz[2]*, Tomasz Lipniacki[1]*

[1] Institute of Fundamental Technological Research, Polish Academy of Sciences, Pawińskiego 5B, 02-106 Warsaw, Poland

[2] Institute of Cell Biology, University of Bern, Baltzerstrasse 4, 3012 Bern, Switzerland

* For correspondence: olivier.pertz@izb.unibe.ch (OP); tlipnia@ippt.pan.pl (TL)

Abstract

Many intracellular signaling pathways, including the MAPK/ERK cascade, respond to an external stimulus in a yes-or-no manner. This has been reflected in estimates of the amount of information a single cell can transmit about the amplitude of an applied (and sustained) input signal, which turns out to only slightly exceed 1 bit. More information, however, can potentially be transmitted in response to time-varying stimulation. In this work, we find a lower bound of the MAPK/ERK signaling channel capacity. We use an epithelial cell line expressing an ERK activity reporter and an optogenetically modified fibroblast growth factor receptor, which allows triggering eventual ERK activity by short light pulses. We observe that it is possible to reconstruct the stimulatory input pattern with five-minute delay and one-minute resolution. By stimulating the cells with random pulse trains we demonstrate that the information transmission rate through the MAPK/ERK pathway can exceed 6 bits per hour. Such high information transmission rate allows the MAPK/ERK pathway to coordinate multiple processes including cell movement.

Introduction

Cells communicate with each other and constantly monitor their extracellular milieu. Upon receiving a stimulus, cells have to recognize its identity and act accordingly to operate in a coordinated manner and properly adapt to the changing environment. At the molecular level, recognition of a specific signal as well as its reliable transmission and appropriate interpretation involve diverse intracellular processes, primarily post-translational protein modifications and gene expression, both of which are notoriously stochastic (Artyomov et al., 2007; Bowsher and Swain, 2012; Raj and van Oudenaarden, 2008). Also, in part due to the molecular noise, the strength of an incoming signal may verge on the biochemical detection limit (Berg and Purcell, 1977; Lipniacki et al., 2007; Mora and Wingreen, 2010). Consequently, at the single-cell level, major intracellular signaling pathways respond to an external stimulus in a crude all-or-nothing manner (Das et al., 2009; Ferrell and Machleder, 1998; Harding et al., 2005; Markevich et al., 2004; Tay et al., 2010; Turner et al., 2010). The inability of individual cells to resolve the level of stimulation (input amplitude) is reflected in the amount of information about the ligand concentration the signaling pathways can transmit, which has been estimated to only slightly exceed 1 bit (Cheong et al., 2011; Selimkhanov et al., 2014; Tang et al., 2021; Tudelska et al., 2017). One bit of information is sufficient to digitally switch on the expression of a pathway-specific set of genes (Rivière et al., 1998; Tay et al., 2010), but insufficient to control signaling-regulated processes that occur at time scales shorter than that of gene expression such as cell migration.

Cell signaling is implemented with biochemically diverse processes that are associated with vastly different time scales: triggering protein production requires about an hour, and as such is relatively the slowest process; protein post-translational modifications require minutes; intracellular ion release-based processes may occur at the subsecond timescale; and neural signal transduction occurs within milliseconds. The time scales associated with these processes translate to the number of bits processed per hour but it is the eventual signaling outcome that determines the necessary amount of information or information transmission rate. Specifically, when the major function of a pathway is regulation of expression of particular genes in response to a stimulus, then quantification of information extracted about the stimulus may be the right way to characterize the pathway. However, when a pathway can be reactivated and reused may times, then one should ask about the information transmission rate and search for temporal information encoding that may possibly maximize this rate.

With the advent of genetically-encoded live cell reporters (Komatsu et al., 2011; Loewith et al., 2021; Regot et al., 2014; Zhang et al., 2018), it has become widely recognized that major signaling pathways may transcode external stimuli into diverse patterns of activity of signaling proteins (Albeck et al., 2013; Lahav et al., 2004; Nelson et al., 2004). These temporal codes are subsequently translated into specific physiological outcomes (Behar and Hoffmann, 2010; Hao and O'Shea, 2011; Harton et al., 2019; Levine et al., 2013; Purvis and Lahav, 2013; Sen et al., 2020; Yosef and Regev, 2011; Zambrano et al., 2016). The mammalian mitogen-activated protein kinase/extracellular signal-regulated kinase (MAPK/ERK) signaling pathway, in addition to discriminating between transient/sustained growth-factor stimulation (Murphy et al., 2002; Sasagawa et al., 2005; Wilson et al., 2017) and performing its temporal integration (Gillies et al., 2017), is capable of transcoding the growth factor concentration into the frequency of ERK activity pulses (Albeck et al., 2013; Kochańczyk et al., 2017). Subsequently, the pulsatile ERK activity is translated into frequency-dependent signaling programs (Toettcher et al., 2013) or even cell fates (Ryu et al., 2015). Notably, neurons utilize temporal coding (Butts et al., 2007; Gollisch and Meister, 2008; MacKay and McCulloch, 1952), and the information transmission rate of a neural spike train may reach tens of bits per second (Arnold et al., 2013; Strong et al., 1998).

Cells are subjected to temporally varying stimulation by morphogens, hormones, or cytokines (Apostolou and Thanos, 2008; Heemskerk et al., 2019; Polonsky et al., 1988; Shvartsman et al., 2001). Although such time-varying conditions can be readily reproduced *in vitro* with the use of microfluidics (Ashall et al., 2009; Harton et al., 2019; Sumit et al., 2017) or, at even higher time resolution, optogenetics (Aoki et al., 2017; Bugaj et al., 2017; Toettcher et al., 2011), estimates of the information transmission rate through signaling pathways, from receptor to effector, are missing.

In this study, we estimate the lower bound of the rate of information transmission through the mammalian MAPK/ERK pathway. We use an epithelial cell line with an optogenetically modified fibroblast growth factor receptor (optoFGFR), which allows triggering eventual ERK activity by short light pulses. The cell line is stably transfected with a reporter, which allows fine temporal monitoring of ERK activity. By stimulating cells with random pulse trains, generated with probabilistic algorithms according to three different information encoding strategies, and applying classifier-based decoding, we demonstrate that the information transmission rate through the pathway can exceed 6 bits per hour. When consecutive input pulses are at least 20 min apart, then, based on ERK activity, it is possible to reconstruct the stimulatory pattern with five-minute delay and one-minute resolution.

Results

Information encoding and information transmission rate

The maximal amount of information that can be transmitted through a communication channel per time unit using the best possible input protocol is called the channel capacity C:

$$C = \max_{\text{protocols}} \lim_{\Delta t \to \infty} \frac{I(S,R)}{\Delta t},$$

where $I(S, R)$ is the mutual information between the input (signal) S and the output (response) R in an experiment of duration Δt (Shannon, 1948). In this work, we compute $I(S, R)$ as the difference:

$$I(S,R) = H(S) - H(S|R),$$

where $H(S)$ is the input entropy (the amount of information sent), which in our experimental design can be computed directly from the assumed probabilistic distribution of the pathway-stimulating input sequence; and $H(S|R)$ is the conditional entropy (the amount of information lost), which captures the uncertainty introduced by the channel (understood here as the signaling pathway). The value $H(S|R)$ depends both on the channel and the signal and as such is estimated based on experimental data.

There are multiple ways to encode information in a train of pulses. When the magnitudes of all stimulation pulses are equal, the input can be perceived as a sequence of 0s (no pulse) and 1s (pulse). The input information (or entropy) rate increases with the frequency of pulses, reaching the maximum for binary sequences that have equal probabilities of 0 and 1. However, shorter intervals between pulses imply higher information loss due to imperfect transmission. One should thus expect that there exists an optimum, for which the information transmission rate (or simply bitrate) is maximal.

We applied three types of pulsatile stimulation protocols to estimate the lower bound for the channel capacity of the MAPK/ERK pathway (see Figure 1A and Methods for details). In what we call the *binary encoding protocol*, information is encoded in a sequence of 0s and 1s which are sent at regular time intervals τ_{clock} with equal probabilities. In our experiments, we stimulated cells with light pulses according to a 0/1 sequence of length 19: `1011010011110000101` (containing all possible 16 subsequences of length 4) and its logic negation. In the *interval encoding protocol*, information is encoded in the lengths of intervals between subsequent input light pulses. To maximize the input entropy, the intervals were drawn from a geometric distribution. In the *interval encoding protocol with a minimal gap*, the time intervals were also drawn from a geometric distribution (with the mean interpulse interval τ_{geom}), but the intervals shorter than a minimal interval τ_{gap} were excluded. For each assumed τ_{gap}, we chose τ_{geom} that maximizes the input entropy (see Methods for details).

Compared to the previous protocol, the inclusion of τ_{gap} reduces the input entropy rate, but also increases the percentage of cells identified as responding to a light pulse timely, which facilitates accurate information transmission.

Detection of pulses

To quantify the bitrate through the MAPK/ERK pathway, we used the human mammary epithelial cell line MCF-10A with both an optogenetically modified fibroblast growth factor receptor (optoFGFR) (Dessauges et al., 2021; Gagliardi et al., 2021), which can be activated by blue light (470 nm), and a fluorescent ERK kinase translocation reporter (ERK KTR), which translocates from the nucleus to the cytoplasm when phosphorylated by ERK (Figure 1B). The cells were stimulated with short (100 ms) blue light pulses according to the three types of pulsatile information encoding protocols (Figure 1A). ERK KTR translocation was observed at one-minute resolution and quantified (Figure 1C–D; see Methods and Figure 1—figure supplement 1 for details of the workflow). Signal transduction from optoFGFR to ERK KTR was found to be fast, with the maximal translocation increment (drop of the nuclear ERK KTR fluorescence) observed between 2 and 3 min, maximum translocation at 6 min, and maximal translocation decrement around 11 min after the light pulse (Figure 1E).

Based on the quantified single-cell trajectories of nuclear ERK KTR (Figure 1D), we reconstructed the input sequence of light pulses using a method based on the *k*-nearest neighbors algorithm (see Methods for details) and data within just the 8 min-wide window sliding over an ERK KTR translocation trajectory. The method was typically able to predict the pulse timing with one-minute resolution (Figure 1F), which is clearly better than any individual pulse feature (*cf*. Figure 1E–F). The percentage of detected pulses increases sharply with the time interval between the pulse to be detected and the previous pulse, reaching about 60% for the interval of 10 min and 90% for the interval of 20 min (Figure 1G). The missed pulses, pulses detected as occurring earlier or later, and false detections are responsible for the information loss.

Bitrate estimation

We estimated the information loss along the pathway by computing the entropy of the input conditioned on its classifier-based reconstruction based on single-cell ERK KTR trajectories. Next, by subtracting the information loss from the input entropy we quantified transmitted information, and eventually by dividing the result by time we were able to estimate the bitrate.

In Figure 2A we show 10 example single-cell ERK KTR translocation trajectories of cells responding to the first sequence used in the binary encoding protocol with the time span between subsequent digits (clock period) τ_{clock} = 10 min. The percentage of cells identified as responding to light pulses varied from 86% to nearly 100%. As expected, the detectability is higher when the time span from the preceding pulse is 20 min or more (more than 95% pulses are detected). A tiny percentage of cells, 1–3%, was identified as responding at time points without a light pulse.

For the binary protocol we performed experiments for 7 different clock periods ranging from 3 to 30 min (Figure 2B). The input information rate, 1 bit/τ_{clock}, decreases with increasing τ_{clock} but, as expected, for longer τ_{clock} the fraction of information lost due to missed pulses or false detections is lower. For the shortest τ_{clock} of 3 min, the input information rate reached 20 bit/h, but due to severe information loss the transmitted information rate was nearly the same as for τ_{clock} = 5 min (Figure 2B). It should be noted that in the case of the binary encoding protocol during input reconstruction we utilize the *a priori* knowledge of the time points in which the light pulses could have occurred ("pulse slots"). Thus, based on the ERK KTR translocation trajectory we have to decide only whether the light pulses occurred in these time points or not. This makes the reconstruction easier than in the interval encoding protocols, however the binary encoding appears rather artificial in the biological context.

In Figure 2C we show representative fragments of ERK KTR translocation trajectories in 10 cells responding to stimulation with light according to the interval encoding protocol with τ_{geom} = 32 min. For all but one input pulse the percentage of cells identified as responding timely exceeds 70% and is generally higher for pulses occurring after a longer time span from a previous pulse. For interpulse intervals below 10 min, the detectability decreases rapidly (for example, for the pulse at minute 744 that occurred 8 min after its predecessor, this fraction happens to be only 21%). For each pulse there is also a fraction of detections that indicate an input pulse 1 min before or after the true pulse. These imprecise detections carry some information about the timing of pulses and thus decrease the bitrate, however less markedly than missed pulses or false detections.

We performed 6 experiments according to the interval encoding protocol with τ_{geom} ranging from 22 to 55 min (Figure 2D). The highest bitrate of 6.3 bit/h was found for τ_{geom} = 35 min, while for τ_{geom} = 31 and 42 min the bitrate was found equal 5.4 and 5.2 bit/h, respectively. The shortest (22 min) and longest (55 min) average intervals resulted in, respectively, the highest and the lowest information loss. This causes that for these two suboptimal protocols, having respectively high (15 bit/h) and low (7.7 bit/h) input information rate, the bitrate is nearly the same, slightly over 5 bit/h.

In Figure 2E, we show 10 example trajectories for the interval encoding protocol with τ_{geom} = 10 min and a gap of τ_{gap} = 20 min (giving together the mean interpulse interval equal 30 min). The ERK KTR translocation pulses are well distinguishable and thus in around 90% of single-cell trajectories the stimulation pulses were reconstructed with one-minute resolution. For this protocol the bitrate was found to be the highest, equal 7.0 bit/h based on two experimental replicates (Figure 2F). The somewhat lower bitrate of 6.1 bit/h was found for the protocol with τ_{geom} = 8 min and τ_{gap} = 15 min (average of two replicates). It is important to stress that in our method of pulse detection based only on the 8-min rolling window we do not use prior information about the gap.

Latency and accuracy of signal detection

In Figure 3A–C we gathered all the experiments to estimate the maximum bitrate that can be achieved across all 3 protocols. From 6 to 9 experiments performed for each protocol we selected 3 (4 for the third protocol) experiments for which we obtained the highest bitrate, and estimated the lower bound of the maximum bitrate as the average over these selected experiments. As a result we obtained the following bounds (mean +/- standard error of the mean):

(1) 4.4 +/− 0.1 bit/h for the binary encoding protocol with the optimal clock period (τ_{clock}) in the range of 3–7 min,

(2) 5.6 +/− 0.2 bit/h for the interval encoding protocol with the optimal average interval (τ_{geom}) in the range of 31–42 min, and

(3) 6.6 +/− 0.2 bit/h for the interval encoding protocol with a minimal gap, with the optimal gap interval (τ_{gap}) in the range of 15–20 min and the (inverse of the) corresponding geometric distribution parameter (τ_{geom}) in the range of 8–10 min.

Altogether, the above results show that the channel capacity of the MAPK/ERK pathway exceeds 6 bit/h and suggest that the highest bitrate can be achieved for the interval encoding protocol with a gap.

We should mention that the bitrate estimations presented in Figure 2 and Figure 3A–C were obtained after rejecting the fraction f = 20% of ERK KTR trajectories that exhibit the lowest variability, that is, those with the smallest average square change of the nuclear intensity between subsequent snapshots. As we can see in Figure 3—figure supplement 1, the maximum bitrate estimated for each of three protocols is an increasing function of f for f in the range from 0 to 50%. In the case of the binary encoding protocol the maximum bitrate increases nearly linearly with f, which is the consequence that for this protocol, for short clock periods lower variability directly corresponds to lower chance of responding to a light pulse. However, for the interval encoding protocol the most significant increase is observed

in the range 0–20%, which motivated us to remove 20% trajectories. At least some of these trajectories come from cells with optoFGFR or ERK KTR not functioning properly.

In Figure 3—figure supplement 2 we show the histograms of bitrate measured for single cells in all experiments. The orange area in the histograms corresponds to the removed 20% fraction of cells. We can notice that the histograms for the interval encoding protocol with a minimal gap are bimodal, but by removing the 20% of cells we may eradicate the lower mode, which additionally justifies the choice of the particular value of f (for consistency we removed the same fraction of trajectories from experiments for the other two protocols).

All bitrate estimations are based on the ERK KTR translocation trajectory analyzed in an 8 min-wide rolling window that ends t_D = 5 min after the hypothetical pulse to be detected (t_D stands for 'time to decision'). This means that we account for information that is available for each cell 5 min after the pulse that the cell is expected to recognize. In Figure 3D we give the maximal bitrate estimates (for the interval encoding protocol with a minimal gap jointly for the experiments with the highest bitrate, encircled in Figure 3A–C) as a function of t_D. We found that increasing t_D beyond 5 min only marginally increases the bitrate, while decreasing it below 3 min dramatically decreases the bitrate (which possibly reflects the fact that the maximum increment is observed between 2 and 3 min after the pulse).

Discussion

Toettcher et al. (2013) showed that the RAS–ERK module of the MAPK pathway may transmit input signals across a broad range of timescales, from 4 min to multiple hours. Here, we explicitly estimated the information transmission rate from FGFR to an ERK activity reporter to find that the MAPK/ERK channel capacity exceeds 6 bit/h. We analyzed three protocols to encode information: binary encoding, interval encoding, and interval encoding with a minimal gap, to find that interval-encoded information can be transmitted at a significantly higher bitrate than binary-encoded information. The presence of a minimal gap between pulses of length comparable to the refractory time (i.e., time in which the cell may not unambiguously respond to a subsequent pulse) further increases the bitrate. The interval encoding appears the most natural from the biological perspective as it assumes that pulses occur independently according to a Poisson process. These random pulses can be associated with single-cell apoptosis, which recently has been found to trigger synchronous ERK activation (Valon et al., 2021) that propagates radially for about three cell "layers" (Gagliardi et al., 2021). Long-distance waves of ERK activity assist wound healing, inducing collective cell migration (Aoki et al., 2017; Hiratsuka et al., 2015). One could expect that even if such waves are initiated with high frequency, the first "layer" of cells filters out pulses

that occur within the refractory time, and thus the further "layers" of cells will be subjected to stimulation that resembles the interval encoding with a minimal gap.

We found that for the interval encoding with a minimal gap the bitrate may exceed 6 bit/h, which imposes a lower bound on the MAPK/ERK channel capacity. The fact that the interval encoding is associated with the highest bitrate follows from the cells' ability to respond to light pulses in a very synchronous manner. The light pulses can be detected nearly perfectly with one-minute resolution (provided that the time from the preceding pulse is longer than the refractory time), based on ERK activity in an 8-min interval ending 5 min after the light pulse. We should notice that because of technical constraints we have not investigated signaling with resolution finer than 1 min, and thus we may not rule out that the MAPK/ERK channel capacity significantly exceeds the determined lower bound of 6 bit/h.

Cells of multicellular organisms send, receive, and process information. Early studies demonstrated that signaling cascades can transmit to transcription factors merely above a bit of information about a cytokine level (Selimkhanov et al., 2014; Sen et al., 2020). Information about the level of stimulation, available to the observer of single-cell responses, is reduced due to extrinsic noise (phenotypic variability), which causes that cells respond differently (but potentially reproducibly) to the same stimuli (Tay et al., 2010; Topolewski et al., 2022; Zhang et al., 2017). In the case of TNF to NF-κB signaling, information is degraded also along the pathway due to intrinsic noise and signal saturability (Tudelska et al., 2017). Consequently, at the transcription factor level, cells may only recognize the presence or absence of a stimulus, not the strength of stimulation. This is sufficient to trigger all-or-nothing gene activation, but insufficient to coordinate a more complex cell behavior.

The MAPK/ERK channel, however, is known to coordinate diverse complex behaviors and cell fate decisions, such as cell proliferation, differentiation, migration, senescence and apoptosis (Sun et al., 2015). Importantly the RAS-to-ERK cascade transmits signals from numerous inputs to numerous outputs regulated by ERK and its upstream components, MEK, RAF, and RAS. It is thus natural to expect that more information may be contained in the time profile of ERK (Rauch et al., 2016; Ryu et al., 2015). In particular, the spatially localized RAS activation is responsible for formation of cell protrusions (Sasaki et al., 2004), which arise and contract in the time scale of a couple of minutes (Yang et al., 2018), enabling cell motion. Since ERK works as a RAS-activated (via RAF and MEK) RAS inhibitor (Zhan et al., 2020), the ERK activity profile influences temporal characteristics of protrusions and thus cell motion. The high information capacity of the MAPK/ERK channel demonstrated in this study enables coordination of versatile functions associated with ERK

and its upstream kinases, with cell motion likely being the process the most information is fed into.

Methods

Experimental methods

Cell culture

The MCF-10A human mammary epithelial cells were a gift of J.S. Brugge. The cells were modified to stably express the nuclear marker H2B-miRFP703, the ERK biosensor ERK-KTR-mRuby2 and the optogenetic actuator optoFGFR with inactivation half-time of about 5.5 min. (Dessauges et al., 2021; Gagliardi et al., 2021). The modified MCF-10A cells were cultured in tissue-culture treated plastic flasks and fed with a growth medium composed of DMEM:F12 (1:1) supplemented with horse serum 5%, recombinant human EGF (20 ng/ml, Peprotech), L-glutamine, hydrocortisone (0.5 µg/ml, Sigma-Aldrich/Merck), insulin (10 µg/ml, Sigma-Aldrich/Merck), penicillin (200 U/ml) and streptomycin (200 µg/ml). The cells were routinely split upon reaching ~90% confluency. For time-lapse optogenetic experiments, cells were seeded on 24-well 1.5 glass bottom plates (Cellvis) coated with 5 µg/ml fibronectin (PanReac AppliChem) at 1×10^5 cells/well density in growth medium two days before the experiment. Four hours before the optogenetic stimulation (2.5 h before imaging), cells were washed twice with PBS and then cultured in a starvation medium composed of DMEM:F12 (1:1) supplemented with BSA (0.3% Sigma-Aldrich/Merck), L-glutamine, hydrocortisone (0.5 µg/ml, Sigma-Aldrich/Merck).

Optogenetic stimulation

OptoFGFR was stimulated with pulses of blue LED light (100 ms, 470 nm, 3 W/cm^2) applied according to specific stimulation protocols (see a further subsection on stimulation protocols).

Imaging

Imaging experiments were performed on an epifluorescence Eclipse Ti inverted fluorescence microscope (Nikon) controlled by NIS-Elements (Nikon) with a Plan Apo air 20× (NA 0.8) objective. Laser-based autofocus was used throughout the experiments. Image acquisition was performed with an Andor Zyla 4.2 plus camera at the 16-bit depth every 1 min. The following excitation and emission filters were used: far red: 640 nm, ET705/72m; red: 555 nm, ET652/60m; green: 470 nm, ET525/36m. Imaging started 1.5 h before the onset of optogenetic stimulation (to provide proper history for ERK KTR track normalization, see a further subsection on signal processing).

Theoretical and computational methods

Stimulation protocols

In the case of binary encoding, all stimulation protocols have 19 temporally equidistant pulse "slots". We applied the following fixed pattern of pulses: `1011010011110000101` (1=pulse, 0=no pulse), which is the shortest sequence containing uniquely every possible subsequence of four binary digits. For each "clock period" (i.e., time between pulse slots) this sequence (in one field of view) and its logic negation (in another field of view) were used. Since the clock periods ranged from 3 min to 30 min, overall protocol durations ranged from 19×3=57 to 19×30=570 min. The estimated values of the information transmission rate are means computed for tracks obtained from 2 fields of view and 4–5 biological replicates for each clock period, except for the clock periods of 20 min and 30 min, for which 10 fields of view from a single biological replicate were used.

In the case of interval encoding, the interpulse intervals were chosen in an randomized manner: the interval lengths were first selected to best reflect the underlying distribution, either geometric or geometric with a minimal gap, given the time budget of a single experiment (~26 h), and then randomly shuffled. A four hour-long resting period was added in the middle of the experiment to allow the cells to regenerate in 3 of 6 experiments with stimulation according to the protocol without a gap and 5 of 9 experiments with stimulation according to the protocol with a minimal gap; however, no significant difference was observed between results of the experiments with and without the resting period. The resting period and the initial 90-min starvation period were excluded from the analysis. The first pulse of the sequence and the first pulse after the resting period were also discarded as non-representative. Overall, in each protocol there were 24–131 analyzed pulses (during 25–31 h) depending on the assumed average interval between pulses.

Nuclei detection and cell tracking

The nuclei were detected in the channel of fluorescently tagged histone 2B (H2B)-miRFP703 using local thresholding. Outlines of overlapping nuclei were split based on geometric convexity defects when possible. Outlines of nuclei that were partially out of frame were excluded from analysis. The nuclei were tracked automatically using a greedy algorithm based on parameters such as proximity of outlines in subsequent time points, their surface area, eccentricity, orientation, total fluorescence intensity and intensity distribution. ERK KTR tracks were obtained by calculating within each tracked nuclear outline the mean intensity in the ERK KTR channel. All image processing was performed within our custom software, SHUTTLETRACKER (`https://pmbm.ippt.pan.pl/software/shuttletracker`).

Signal processing

For each tracked nucleus, the mean ERK KTR intensity in its contour was quantified and normalized, first with the whole-image mean intensity in the ERK KTR channel (to compensate for possible global changes in fluorescence), and then with the average over the cell 120-min history (to account for variation in ERK KTR expression or its uneven visibility in individual cells). Such normalized values are subtracted from 1 and then referred to simply as 'ERK KTR translocation' and denoted x_t, where t indicates a time point and directly corresponds to the minute of the imaged part of the experiment. Of note, for nuclear ERK KTR signal constant in time, such normalization and linear transformation imply conveniently that $x_t = 0$.

Selection of tracks

In each field of view, we ranked tracks by their length and then by their quality, defined as low variation of the nuclear area within the track, and preselected 500 top scoring tracks. To eliminate cells that responded weakly to stimulation, for example due to low reporter expression, we further rejected 100 tracks (20%) with the lowest sum-of-squares of the discrete derivative of the ERK KTR translocation trajectory (computed after only the first step of normalization).

Input reconstruction

Binary encoding. The ERK KTR translocation trajectories from each experiment were split into the training set (200 randomly selected trajectories) and the test set (remaining 200 trajectories). For each potential light pulse time point t_0, referred to as "slot", we extracted slices of $\ell = 6$ subsequent time points beginning at three different one-minute shifts with respect to t_0: 2 min before the slot (that is, from $t_0 - 2$ to $t_0 + 3$), 1 min before the slot (from $t_0 - 1$ to $t_0 + 4$), and exactly on the time point of the slot (from t_0 to $t_0 + 5$). For each slice we computed $\ell - 1$ discrete backward derivatives, $\Delta x_t = x_t - x_{t-1}$. Separately for each of three sets of slices (corresponding to a specific shift with respect to t_0), a k-nearest neighbors ($k = 10$) classifier (Pedregosa et al., 2011) with $(\ell - 1)$-dimensional Euclidean distance and inverse-distance weighting was trained such that each slice is labeled with 0/1 depending on the predicted occurrence of a light pulse in its slot. In this way, three 0/1 labels are assigned to a single slot. To obtain input signal reconstruction in each slot of x_t, an ensemble classifier combined three binary predictions through hard voting. In the estimation of the confusion matrix (described further), the whole procedure was repeated for 5 random partitionings of trajectories into the training set and the test set. We checked that the reconstruction is not improved for higher k.

Interval encoding. The ERK KTR translocation trajectories from each experiment were split into the training set (200 randomly selected trajectories) and the test set (200 remaining trajectories). Each trajectory was represented as a set of overlapping slices of $\ell = 6$ subsequent time points. The slices constitute a perfect 6-fold coverage meaning that each (non-terminal) time point belongs to 6 (partially overlapping) slices. Each slice was labeled with the "time after pulse" (TAP) being the time from the last light pulse to the last time point of the slice (or from the previous pulse if this time is shorter than 3 min); this adjustment is important in the case of very short, 3–4 min, interpulse intervals). For each slice we computed $\ell - 1$ discrete backward derivatives, $\Delta x_t = x_t - x_{t-1}$. A k-nearest neighbors ($k = 10$) classifier (Pedregosa et al., 2011) with $(\ell - 1)$-dimensional Euclidean distance and inverse-distance weighting was trained to predict a TAP associated with each slice. Slices with TAP values of 3, 4, or 5 min were used to predict pulses through hard voting: time points indicated by at least two of three slices were considered as time points having a light pulse in the final reconstruction (see Figure 1—figure supplement 2). To additionally prevent a single pulse from being predicted multiple times, if more than one prediction was indicated within any three subsequent time points, all predictions except the first one were discarded. In the estimation of the contingency table (described further), the whole procedure was repeated for 5 different random partitionings of trajectories into the test set and the train set.

Let us notice that in both the binary and the interval encoding protocols, the decision whether to classify a given time point t_0 as a point containing a light pulse was made based on 3 subsequent, partially overlapping slices of length 6, which cover 8 subsequent values of x_t (for t ranging from $t_0 - 2$ to $t_0 + 5$). Thus, only information available to a cell 5 min after the pulse was used by the trained ensemble classifier to make a prediction. In Figure 3D–E, the length of this window is varied to check how fast information is accumulated.

Bitrate computation

We estimated the bitrate as the amount of information $I(S, R)$ between the input signal S and the elicited response R sent within an interval corresponding to the total input duration Δt according to the formula:

$$i(S,R) = \frac{I(S,R)}{\Delta t} = \frac{H(S) - H(S|R)}{\Delta t} = \frac{H(S)}{\Delta t} - \frac{H(S|R)}{\Delta t}, \qquad (1)$$

where $H(S)$ is the entropy of an input signal and $H(S|R)$ is the entropy of the input conditioned on the response (or, in our case, on the output-based reconstruction of the input). As described below, the input entropy rate, $h(S) := H(S)/\Delta t$, may be determined theoretically, whereas the conditional entropy $H(S|R)$ is calculated based on ERK KTR translocation trajectories.

Input entropy rate

In the case of the binary encoding protocol, input sequences contain 0/1 digits occurring independently with identical probabilities of ½ in temporally equidistant pulse slots. The entropy of such 19-digit input sequences is $H_{\text{binary}}(S)$ = 19 bits. When digits occur in pulse slots τ_{clock} apart, then the input entropy rate per digit is

$$h_{\text{binary}}(S;\tau_{\text{clock}}) = \frac{19 \text{ bits}}{19\,\tau_{\text{clock}}} = 1 \text{ bit}/\tau_{\text{clock}}. \quad (2)$$

Since τ_{clock} is the clock period of the binary encoding protocol, Eq. (2) expresses the input entropy rate per clock period.

In the case of the interval encoding protocols, intervals between pulses are drawn by random from the geometric distribution with the rate parameter $p = 1/\tau_{\text{geom}}$ and are optionally lengthened by adding τ_{gap}. The entropy of the geometric distribution is

$$-\frac{p\log_2 p + (1-p)\log_2(1-p)}{p} = \tau_{\text{geom}}\log_2\tau_{\text{geom}} - (\tau_{\text{geom}}-1)\log_2(\tau_{\text{geom}}-1), \quad (3)$$

so the entropy rate $h_{\text{interval}}(S; \tau_{\text{geom}}, \tau_{\text{gap}})$ is

$$h_{\text{interval}}(S;\tau_{\text{geom}},\tau_{\text{gap}}) = \frac{\tau_{\text{geom}}\log_2\tau_{\text{geom}} - (\tau_{\text{geom}}-1)\log_2(\tau_{\text{geom}}-1)}{\tau_{\text{geom}}+\tau_{\text{gap}}}, \quad (4)$$

where $\tau_{\text{geom}} + \tau_{\text{gap}}$ is the mean interpulse interval. Since in the interval encoding protocols, digits 0/1 occur at the one-minute resolution, h_{interval} computed in Eq. (4) is also the entropy per digit. For the "gapless" protocol, τ_{geom} was varied whereas τ_{gap} was set to 2 min (to avoid ambiguities in signal reconstruction). For τ_{geom} > 3.15 min, $h_{\text{interval}}(S; \tau_{\text{geom}}, \tau_{\text{gap}})$ is a decreasing function of τ_{geom}. For the protocol with a minimal gap, τ_{gap} was varied and τ_{geom} was adjusted through numerical optimization to maximize $h_{\text{interval}}(S; \tau_{\text{geom}}, \tau_{\text{gap}})$.

Conditional entropy

For the binary and the interval encoding protocols we estimate from above the conditional entropy $H(S|R)$ per digit of the input given its reconstruction. In light of Eq. (1) this will provide us with a lower bound on the bitrate $i(S, R)$. Entropy of a joint distribution is lower than the sum of individual entropies (Cover and Thomas, 2006), thus

$$H(S|R) \leq \sum_d H(S_d|R), \quad (5)$$

where S_d is a single input digit and $H(S_d|R)$ is the entropy of that input digit conditioned on the whole-sequence reconstruction R. The equality holds only when R and S jointly are a Markov process, this is, when digits occur independently and the reconstruction of a given digit does not depend on other digits. Of note, in our experiments the input digits are independent for the binary encoding protocol, but dependent for the interval encoding protocol with a (minimal) gap. However, even for the binary encoding protocol, the probability of detecting a pulse (digit '1') depends on the time interval from the previous 1.

Further, from the data processing inequality (Cover and Thomas, 2006), for the binary encoding protocol, we have

$$H(S_d|R) \leq H(S_d|R_d), \quad (6)$$

where $H(S_d|R_d)$ is the entropy of an input digit S_d conditioned on its reconstruction R_d, and for the interval encoding protocols we have

$$H(S_d|R) \leq H(S_d|\,(R_{d-1}, R_d, R_{d+1})), \quad (7)$$

where $H(S_d|(R_{d-1}, R_d, R_{d+1}))$ is the entropy of S_d conditioned on three subsequent digits of the reconstruction.

Taken together, from inequalities (5)–(7) we have

$$H(S|R) \leq \sum_d H(S_d|R_d) \quad \text{and} \quad H(S|R) \leq \sum_d H(S_d|\,(R_{d-1}, R_d, R_{d+1})), \quad (8)$$

which means that to obtain upper bounds on conditional entropies for the binary encoding and the interval encoding protocols we have to calculate $H(S_d|R_d)$ and $H(S_d|(R_{d-1}, R_d, R_{d+1}))$, respectively.

Calculation of $H(S_d|R_d)$ for binary encoding. To obtain $H(S_d|R_d)$, we calculated the confusion matrix between S_d and R_d:

S_d \ R_d	**1**	**0**
1	TP	FN
0	FP	TN

where TP, FP, FN, TN are, respectively, the probabilities of true positive detections, false positive detections ("false detections"), false negative detections ("missed pulses"), and true negative detections averaged over all time points, all selected tracks, and all partitions of data into the train set and the test set. Based on this confusion matrix we calculated $H(S_d|R_d)$ according to the definition as:

$$H(S_d|\,R_d) = -\mathbb{E}(\log_2 p(S_d|R_d)) = -\sum_{s,r\in\{0,1\}} p(S_d = s, R_d = r)\, \log_2 \frac{p(S_d=s, R_d=r)}{p(R_d=r)}. \quad (9)$$

Calculation of $H(S_d|(R_{d-1}, R_d, R_{d+1}))$ for interval encoding. For this encoding, we computed the contingency table showing the relation between S_d and the reconstruction of the three subsequent digits (R_{d-1}, R_d, R_{d+1}), which also accounts for information carried by inaccurate detections:

S_d \ (R_{d-1}, R_d, R_{d+1})	(0,0,0)	(1,0,0)	(0,1,0)	(0,0,1)
1				
0				

The entries of the contingency table are joint probabilities $p(S_d = s, (R_{d-1}, R_d, R_{d+1}) = (r_{-1}, r_0, r_{+1}))$ of input signal $s \in \{0, 1\}$ and reconstructed input $r \in \{(0,0,0), (1,0,0), (0,1,0), (0,0,1)\}$. In contrast to the confusion matrix for the binary encoding, these joint probabilities have no straightforward interpretation in terms of TP, FP, FN, TN or inaccurate detection probabilities. The combinations of (R_{d-1}, R_d, R_{d+1}) containing two or three 1s do not occur due to the prior elimination of detections that are closer than 3 min apart. The conditional entropy was calculated according to the definition as:

$$H(S_d|\,(R_{d-1}, R_d, R_{d+1})) = -\sum_{s, r_{-1}, r_0, r_{+1} \in \{0,1\}} p(S_d = s, (R_{d-1}, R_d, R_{d+1}) = (r_{-1}, r_0, r_{+1})) \times \log_2 \frac{p(S_d = s, (R_{d-1}, R_d, R_{d+1}) = (r_{-1}, r_0, r_{+1}))}{p((R_{d-1}, R_d, R_{d+1}) = (r_{-1}, r_0, r_{+1}))}. \quad (10)$$

To summarize, bitrate may be computed based on Eq. (1) with input entropy rates given by Eq. (2) and Eq. (3) and conditional entropies given by Eq. (9) and Eq. (10) in the case of the binary encoding protocols and in the case of interval encoding protocols, respectively.

Sources of information loss

To determine the sources of the information loss (Figure 2BDF), we sequentially corrected all types of errors in the reconstruction: false detections (false positives), missed pulses (false negatives), and for the interval encoding protocols also inaccurate (deferred or advanced) detections. After each correction step, we recomputed the confusion matrix/contingency table and attributed the decrease of conditional entropy and the resulting increases of bitrate to the particular type of error. Since the obtained results depend on a particular order of correction steps, to compare individual contributions from the three corresponding types of reconstruction errors, we calculated each of these contributions by averaging over all possible orders of the correction steps (2 permutations for the binary encoding protocol, 6 permutations for the interval encoding protocols; see Figure 2—figure supplement 1). Of note, each sequence of correction steps restores exactly the input signal

and the estimated bitrate losses associated with considered error types sum up to the total bitrate loss. Since the procedure is symmetric with respect to each type of error, these contributions may be compared.

Funding

National Science Centre grant 019/35/B/NZ2/03898 to Tomasz Lipniacki.
Swiss National Science Foundation grant Div3 310030_185376 to Olivier Pertz.

Acknowledgments

We thank Prof. Joan S. Brugge from Harvard Medical School, Boston, MA for providing the MCF-10A human mammary epithelial cells line. We acknowledge support of the Swiss Cancer League and the Microscopy Imaging Center of the University of Bern (https://www.mic.unibe.ch).

Authors contributions

Paweł-Nałęcz Jawecki, Conceptualization, Investigation, Writing – original draft; Paolo Armando Gagliardi, Conceptualization, Investigation, Writing – review and editing; Marek Kochańczyk, Conceptualization, Data curation, Methodology, Software, Writing – original draft, Writing – original review and editing; Coralie Dessauges, Methodology, Resources; Olivier Pertz, Conceptualization, Funding acquisition; Tomasz Lipniacki, Conceptualization, Funding acquisitions, Writing – original draft, Writing – original review and editing.

References

Albeck JG, Mills GB, Brugge JS. 2013. Frequency-modulated pulses of ERK activity transmit quantitative proliferation signals. *Mol Cell* **49**:249–261. doi:10.1016/j.molcel.2012.11.002

Aoki K, Kondo Y, Naoki H, Hiratsuka T, Itoh RE, Matsuda M. 2017. Propagating wave of ERK activation orients collective cell migration. *Dev Cell* **43**:305-317.e5. doi:10.1016/j.devcel.2017.10.016

Apostolou E, Thanos D. 2008. Virus Infection Induces NF-κB-dependent interchromosomal associations mediating monoallelic IFN-β gene expression. *Cell* **134**:85–96. doi:10.1016/j.cell.2008.05.052

Arnold MM, Szczepanski J, Montejo N, Amigó JM, Wajnryb E, Sanchez-Vives MV. 2013. Information content in cortical spike trains during brain state transitions. *Journal of Sleep Research* **22**:13–21. doi:10.1111/j.1365-2869.2012.01031.x

Artyomov MN, Das J, Kardar M, Chakraborty AK. 2007. Purely stochastic binary decisions in cell signaling models without underlying deterministic bistabilities. *Proc Natl Acad Sci USA* **104**:18958–18963. doi:10.1073/pnas.0706110104

Ashall L, Horton CA, Nelson DE, Paszek P, Harper CV, Sillitoe K, Ryan S, Spiller DG, Unitt JF, Broomhead DS, Kell DB, Rand DA, Sée V, White MRH. 2009. Pulsatile stimulation determines timing and specificity of NF-κB-dependent transcription. *Science* **324**:242–246. doi:10.1126/science.1164860

Behar M, Hoffmann A. 2010. Understanding the temporal codes of intra-cellular signals. *Curr Opin Genet Dev* **20**:684–693. doi:10.1016/j.gde.2010.09.007

Berg HC, Purcell EM. 1977. Physics of chemoreception. *Biophys J* **20**:193–219. doi:10.1016/S0006-3495(77)85544-6

Bowsher CG, Swain PS. 2012. Identifying sources of variation and the flow of information in biochemical networks. *Proc Natl Acad Sci USA* **109**:E1320-1328. doi:10.1073/pnas.1119407109

Bugaj LJ, O'Donoghue GP, Lim WA. 2017. Interrogating cellular perception and decision making with optogenetic tools. *J Cell Biol* **216**:25–28. doi:10.1083/jcb.201612094

Butts DA, Weng C, Jin J, Yeh C-I, Lesica NA, Alonso J-M, Stanley GB. 2007. Temporal precision in the neural code and the timescales of natural vision. *Nature* **449**:92–95. doi:10.1038/nature06105

Cheong R, Rhee A, Wang CJ, Nemenman I, Levchenko A. 2011. Information transduction capacity of noisy biochemical signaling networks. *Science* **334**:354–358. doi:10.1126/science.1204553

Cover TM, Thomas JA. 2006. Elements of information theory, 2nd ed. ed. Hoboken, N.J: Wiley-Interscience.

Das J, Ho M, Zikherman J, Govern C, Yang M, Weiss A, Chakraborty AK, Roose JP. 2009. Digital signaling and hysteresis characterize Ras activation in lymphoid cells. *Cell* **136**:337–351. doi:10.1016/j.cell.2008.11.051

Dessauges C, Mikelson J, Dobrzyński M, Jacques M-A, Frismantiene A, Gagliardi PA, Khammash M, Pertz O. 2021. Optogenetic actuator/biosensor circuits for large-scale interrogation of ERK dynamics identify sources of MAPK signaling robustness. doi:10.1101/2021.07.27.453955

Ferrell JE, Machleder EM. 1998. The biochemical basis of an all-or-none cell fate switch in Xenopus oocytes. *Science* **280**:895–898. doi:10.1126/science.280.5365.895

Gagliardi PA, Dobrzyński M, Jacques M-A, Dessauges C, Ender P, Blum Y, Hughes RM, Cohen AR, Pertz O. 2021. Collective ERK/Akt activity waves orchestrate epithelial homeostasis by driving apoptosis-induced survival. *Dev Cell* **56**:1712-1726.e6. doi:10.1016/j.devcel.2021.05.007

Gillies TE, Pargett M, Minguet M, Davies AE, Albeck JG. 2017. Linear integration of ERK activity predominates over persistence detection in Fra-1 regulation. *Cell Syst* **5**:549-563.e5. doi:10.1016/j.cels.2017.10.019

Gollisch T, Meister M. 2008. Rapid neural coding in the retina with relative spike latencies. *Science* **319**:1108–1111. doi:10.1126/science.1149639

Hao N, O'Shea EK. 2011. Signal-dependent dynamics of transcription factor translocation controls gene expression. *Nat Struct Mol Biol* **19**:31–39. doi:10.1038/nsmb.2192

Harding A, Tian T, Westbury E, Frische E, Hancock JF. 2005. Subcellular localization determines MAP kinase signal output. *Current Biology* **15**:869–873. doi:10.1016/j.cub.2005.04.020

Harton MD, Koh WS, Bunker AD, Singh A, Batchelor E. 2019. p53 pulse modulation differentially regulates target gene promoters to regulate cell fate decisions. *Mol Syst Biol* **15**:e8685. doi:10.15252/msb.20188685

Heemskerk I, Burt K, Miller M, Chhabra S, Guerra MC, Liu L, Warmflash A. 2019. Rapid changes in morphogen concentration control self-organized patterning in human embryonic stem cells. *Elife* **8**:e40526. doi:10.7554/eLife.40526

Hiratsuka T, Fujita Y, Naoki H, Aoki K, Kamioka Y, Matsuda M. 2015. Intercellular propagation of extracellular signal-regulated kinase activation revealed by in vivo imaging of mouse skin. *eLife Sciences* **4**:e05178. doi:10.7554/eLife.05178

Kochańczyk M, Kocieniewski P, Kozłowska E, Jaruszewicz-Błońska J, Sparta B, Pargett M, Albeck JG, Hlavacek WS, Lipniacki T. 2017. Relaxation oscillations and hierarchy of feedbacks in MAPK signaling. *Sci Rep* **7**:38244. doi:10.1038/srep38244

Komatsu N, Aoki K, Yamada M, Yukinaga H, Fujita Y, Kamioka Y, Matsuda M. 2011. Development of an optimized backbone of FRET biosensors for kinases and GTPases. *Mol Biol Cell* **22**:4647–4656. doi:10.1091/mbc.E11-01-0072

Lahav G, Rosenfeld N, Sigal A, Geva-Zatorsky N, Levine AJ, Elowitz MB, Alon U. 2004. Dynamics of the p53-Mdm2 feedback loop in individual cells. *Nat Genet* **36**:147–150. doi:10.1038/ng1293

Levine JH, Lin Y, Elowitz MB. 2013. Functional roles of pulsing in genetic circuits. *Science* **342**:1193–1200. doi:10.1126/science.1239999

Lipniacki T, Puszynski K, Paszek P, Brasier AR, Kimmel M. 2007. Single TNFα trimers mediating NF-κB activation: stochastic robustness of NF-κB signaling. *BMC Bioinformatics* **8**:376. doi:10.1186/1471-2105-8-376

Loewith R, Roux A, Pertz O. 2021. Chemical-biology-derived in vivo sensors: Past, present, and future. *Chimia* **75**:1017–1021. doi:10.2533/chimia.2021.1017

MacKay DM, McCulloch WS. 1952. The limiting information capacity of a neuronal link. *Bull Math Biophys* **14**:127–135. doi:10.1007/BF02477711

Markevich NI, Hoek JB, Kholodenko BN. 2004. Signaling switches and bistability arising from multisite phosphorylation in protein kinase cascades. *J Cell Biol* **164**:353–359. doi:10.1083/jcb.200308060

Mora T, Wingreen NS. 2010. Limits of sensing temporal concentration changes by single cells. *Phys Rev Lett* **104**:248101. doi:10.1103/PhysRevLett.104.248101

Murphy LO, Smith S, Chen R-H, Fingar DC, Blenis J. 2002. Molecular interpretation of ERK signal duration by immediate early gene products. *Nat Cell Biol* **4**:556–564. doi:10.1038/ncb822

Nelson DE, Ihekwaba AEC, Elliott M, Johnson JR, Gibney CA, Foreman BE, Nelson G, See V, Horton CA, Spiller DG, Edwards SW, McDowell HP, Unitt JF, Sullivan E, Grimley R, Benson N, Broomhead D, Kell DB, White MRH. 2004. Oscillations in NF-κB signaling control the dynamics of gene expression. *Science* **306**:704–708. doi:10.1126/science.1099962

Pedregosa F, Varoquaux G, Gramfort A, Michel V, Thirion B, Grisel O, Blondel M, Prettenhofer P, Weiss R, Dubourg V, Vanderplas J, Passos A, Cournapeau D, Brucher M, Perrot M, Duchesnay É. 2011. Scikit-learn: Machine learning in Python. *Journal of Machine Learning Research* **12**:2825–2830.

Polonsky KS, Given BD, Van Cauter E. 1988. Twenty-four-hour profiles and pulsatile patterns of insulin secretion in normal and obese subjects. *J Clin Invest* **81**:442–448. doi:10.1172/JCI113339

Purvis JE, Lahav G. 2013. Encoding and decoding cellular information through signaling dynamics. *Cell* **152**:945–956. doi:10.1016/j.cell.2013.02.005

Raj A, van Oudenaarden A. 2008. Nature, nurture, or chance: Stochastic gene expression and its consequences. *Cell* **135**:216–226. doi:10.1016/j.cell.2008.09.050

Rauch N, Rukhlenko OS, Kolch W, Kholodenko BN. 2016. MAPK kinase signalling dynamics regulate cell fate decisions and drug resistance. *Curr Opin Struct Biol* **41**:151–158. doi:10.1016/j.sbi.2016.07.019

Regot S, Hughey JJ, Bajar BT, Carrasco S, Covert MW. 2014. High-sensitivity measurements of multiple kinase activities in live single cells. *Cell* **157**:1724–1734. doi:10.1016/j.cell.2014.04.039

Rivière I, Sunshine MJ, Littman DR. 1998. Regulation of IL-4 expression by activation of individual alleles. *Immunity* **9**:217–228. doi:10.1016/s1074-7613(00)80604-4

Ryu H, Chung M, Dobrzyński M, Fey D, Blum Y, Lee SS, Peter M, Kholodenko BN, Jeon NL, Pertz O. 2015. Frequency modulation of ERK activation dynamics rewires cell fate. *Mol Syst Biol* **11**:838. doi:10.15252/msb.20156458

Sasagawa S, Ozaki Y, Fujita K, Kuroda S. 2005. Prediction and validation of the distinct dynamics of transient and sustained ERK activation. *Nat Cell Biol* **7**:365–373. doi:10.1038/ncb1233

Sasaki AT, Chun C, Takeda K, Firtel RA. 2004. Localized Ras signaling at the leading edge regulates PI3K, cell polarity, and directional cell movement. *J Cell Biol* **167**:505–518. doi:10.1083/jcb.200406177

Selimkhanov J, Taylor B, Yao J, Pilko A, Albeck J, Hoffmann A, Tsimring L, Wollman R. 2014. Accurate information transmission through dynamic biochemical signaling networks. *Science* **346**:1370–1373. doi:10.1126/science.1254933

Sen S, Cheng Z, Sheu KM, Chen YH, Hoffmann A. 2020. Gene regulatory strategies that decode the duration of NFκB dynamics contribute to LPS- versus TNF-specific gene expression. *Cell Syst* **10**:169-182.e5. doi:10.1016/j.cels.2019.12.004

Shannon CE. 1948. A Mathematical Theory of Communication. *Bell System Technical Journal* **27**:379–423. doi:10.1002/j.1538-7305.1948.tb01338.x

Shvartsman SY, Wiley HS, Deen WM, Lauffenburger DA. 2001. Spatial range of autocrine signaling: modeling and computational analysis. *Biophys J* **81**:1854–1867. doi:10.1016/S0006-3495(01)75837-7

Strong SP, Koberle R, de Ruyter van Steveninck RR, Bialek W. 1998. Entropy and information in neural spike trains. *Phys Rev Lett* **80**:197–200. doi:10.1103/PhysRevLett.80.197

Sumit M, Takayama S, Linderman JJ. 2017. New insights into mammalian signaling pathways using microfluidic pulsatile inputs and mathematical modeling. *Integr Biol (Camb)* **9**:6–21. doi:10.1039/c6ib00178e

Sun Y, Liu W-Z, Liu T, Feng X, Yang N, Zhou H-F. 2015. Signaling pathway of MAPK/ERK in cell proliferation, differentiation, migration, senescence and apoptosis. *J Recept Signal Transduct Res* **35**:600–604. doi:10.3109/10799893.2015.1030412

Tang Y, Adelaja A, Ye FX-F, Deeds E, Wollman R, Hoffmann A. 2021. Quantifying information accumulation encoded in the dynamics of biochemical signaling. *Nat Commun* **12**:1272. doi:10.1038/s41467-021-21562-0

Tay S, Hughey JJ, Lee TK, Lipniacki T, Quake SR, Covert MW. 2010. Single-cell NF-κB dynamics reveal digital activation and analogue information processing. *Nature* **466**:267–271. doi:10.1038/nature09145

Toettcher JE, Voigt CA, Weiner OD, Lim WA. 2011. The promise of optogenetics in cell biology: interrogating molecular circuits in space and time. *Nat Methods* **8**:35–38. doi:10.1038/nmeth.f.326

Toettcher JE, Weiner OD, Lim WA. 2013. Using optogenetics to interrogate the dynamic control of signal transmission by the Ras/Erk module. *Cell* **155**:1422–1434. doi:10.1016/j.cell.2013.11.004

Topolewski P, Zakrzewska KE, Walczak J, Nienałtowski K, Müller-Newen G, Singh A, Komorowski M. 2022. Phenotypic variability, not noise, accounts for most of the cell-

to-cell heterogeneity in IFN-γ and oncostatin M signaling responses. *Sci Signal* **15**:eabd9303. doi:10.1126/scisignal.abd9303

Tudelska K, Markiewicz J, Kochańczyk M, Czerkies M, Prus W, Korwek Z, Abdi A, Błoński S, Kaźmierczak B, Lipniacki T. 2017. Information processing in the NF-κB pathway. *Sci Rep* **7**:15926. doi:10.1038/s41598-017-16166-y

Turner DA, Paszek P, Woodcock DJ, Nelson DE, Horton CA, Wang Y, Spiller DG, Rand DA, White MRH, Harper CV. 2010. Physiological levels of TNFalpha stimulation induce stochastic dynamics of NF-kappaB responses in single living cells. *J Cell Sci* **123**:2834–2843. doi:10.1242/jcs.069641

Valon L, Davidović A, Levillayer F, Villars A, Chouly M, Cerqueira-Campos F, Levayer R. 2021. Robustness of epithelial sealing is an emerging property of local ERK feedback driven by cell elimination. *Dev Cell* **56**:1700-1711.e8. doi:10.1016/j.devcel.2021.05.006

Wilson MZ, Ravindran PT, Lim WA, Toettcher JE. 2017. Tracing information flow from Erk to target gene induction reveals mechanisms of dynamic and combinatorial control. *Mol Cell* **67**:757-769.e5. doi:10.1016/j.molcel.2017.07.016

Yang J-M, Bhattacharya S, West-Foyle H, Hung C-F, Wu T-C, Iglesias PA, Huang C-H. 2018. Integrating chemical and mechanical signals through dynamic coupling between cellular protrusions and pulsed ERK activation. *Nat Commun* **9**:4673. doi:10.1038/s41467-018-07150-9

Yosef N, Regev A. 2011. Impulse control: Temporal dynamics in gene transcription. *Cell* **144**:886–896. doi:10.1016/j.cell.2011.02.015

Zambrano S, Toma ID, Piffer A, Bianchi ME, Agresti A. 2016. NF-κB oscillations translate into functionally related patterns of gene expression. *eLife Sciences* **5**:e09100. doi:10.7554/eLife.09100

Zhan H, Bhattacharya S, Cai H, Iglesias PA, Huang C-H, Devreotes PN. 2020. An excitable Ras/PI3K/ERK signaling network controls migration and oncogenic transformation in epithelial cells. *Dev Cell* **54**:608-623.e5. doi:10.1016/j.devcel.2020.08.001

Zhang Q, Gupta S, Schipper DL, Kowalczyk GJ, Mancini AE, Faeder JR, Lee REC. 2017. NF-κB dynamics discriminate between TNF doses in single cells. *Cell Syst* **5**:638-645.e5. doi:10.1016/j.cels.2017.10.011

Zhang Q, Huang H, Zhang L, Wu R, Chung C-I, Zhang S-Q, Torra J, Schepis A, Coughlin SR, Kornberg TB, Shu X. 2018. Visualizing dynamics of cell signaling in vivo with a phase separation-based kinase reporter. *Mol Cell* **69**:334-346.e4. doi:10.1016/j.molcel.2017.12.008

Figure captions

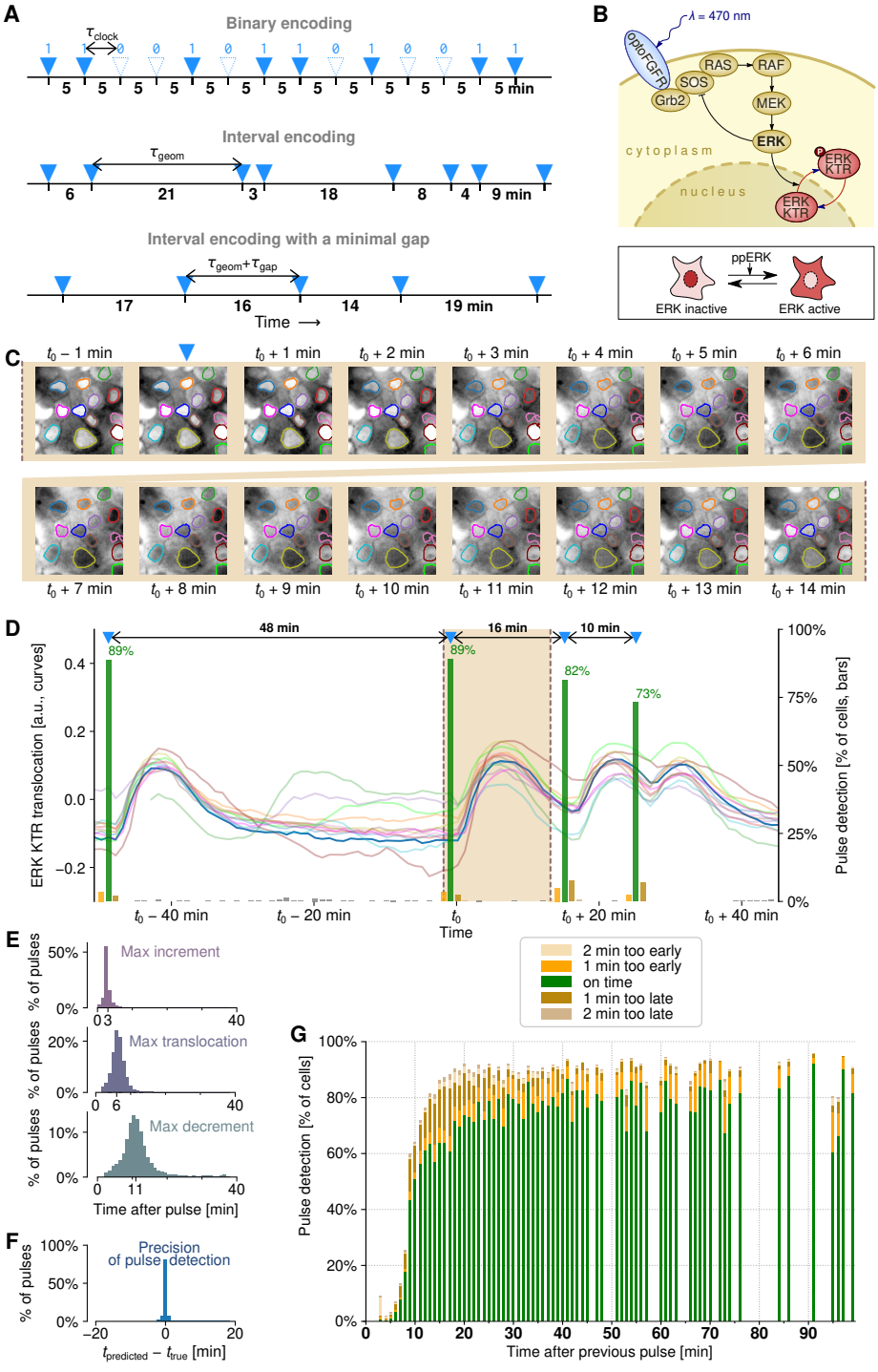

Figure 1. Decoding pulsatile signals relayed through the MAPK/ERK pathway.

(**A**) Input: three considered protocols of encoding information in a pulse train. In binary encoding, a pulse is either present or not in each of the temporally equidistant slots. In interval encoding,

information is carried by the lengths of time intervals between subsequent pulses. The intervals are drawn from a geometric distribution (at the one-minute resolution). In interval encoding with a minimal gap, the intervals are drawn from a geometric distribution and then the intervals shorter than the minimal gap are discarded.

(**B**) Diagram of the MAPK/ERK pathway within the engineered MCF-10A cells. Blue light activates optoFGFR, triggering a kinase cascade, which culminates in ERK activation. The fluorescent (mRuby2) ERK KTR, which in non-stimulated cells is mostly localized to the nucleus, upon phosphorylation by nuclear active ERK (ppERK) is exported to the cytoplasm. (A drop of) the mean nuclear fluorescence of ERK KTR is used as a proxy of its translocation and ERK activity.

(**C**) Output: ERK KTR translocation in response to activation of optoFGFR by a light pulse at t0. Nuclear contours of 13 cells are marked with different colors. For the sake of presentation, microscopic images are normalized such that the original 10%–90% quantiles of pixel intensity span over the whole grayscale range, black to white.

(**D**) Input reconstruction: time track of ERK KTR translocation in 13 representative cells in response to a sequence of 4 light pulses. The shaded interval is the interval in which snapshots shown in panel C were acquired; the trajectories correspond to respective color-coded nuclear outlines shown in panel C. Green bars show the proportion of cells (estimated based on 400 single-cell trajectories) in which a pulse was detected by the trained classifier.

(**E**) Histograms of three basic temporal features characterizing the ERK KTR translocation profile: time to the largest translocation increment, peak of translocation, and the largest translocation decrement (all with respect to the time of a light pulse that elicited the characterized response). In a typical cell, the translocation has the steepest slope between 2 and 3 min after the light pulse, reaches the maximum at 6 min, and rebounds at the highest rate between 10 and 11 min after the light pulse. Data from all 6 experiments with the gapless interval encoding protocol.

(**F**) Accuracy of the light pulse detection. Most of the pulses are detected exactly at one-minute resolution. Data as in panel E, classifier trained on other cells from the same experiment. (G) Proportion of cells in which a pulse was detected as a function of the interval after the previous pulse. Nearly 90% of pulses are detected with 2-min accuracy if occurring at least 15 min after the previous pulse. About 80% of pulses that are more than 20 min apart are detected exactly. Data as in panel F.

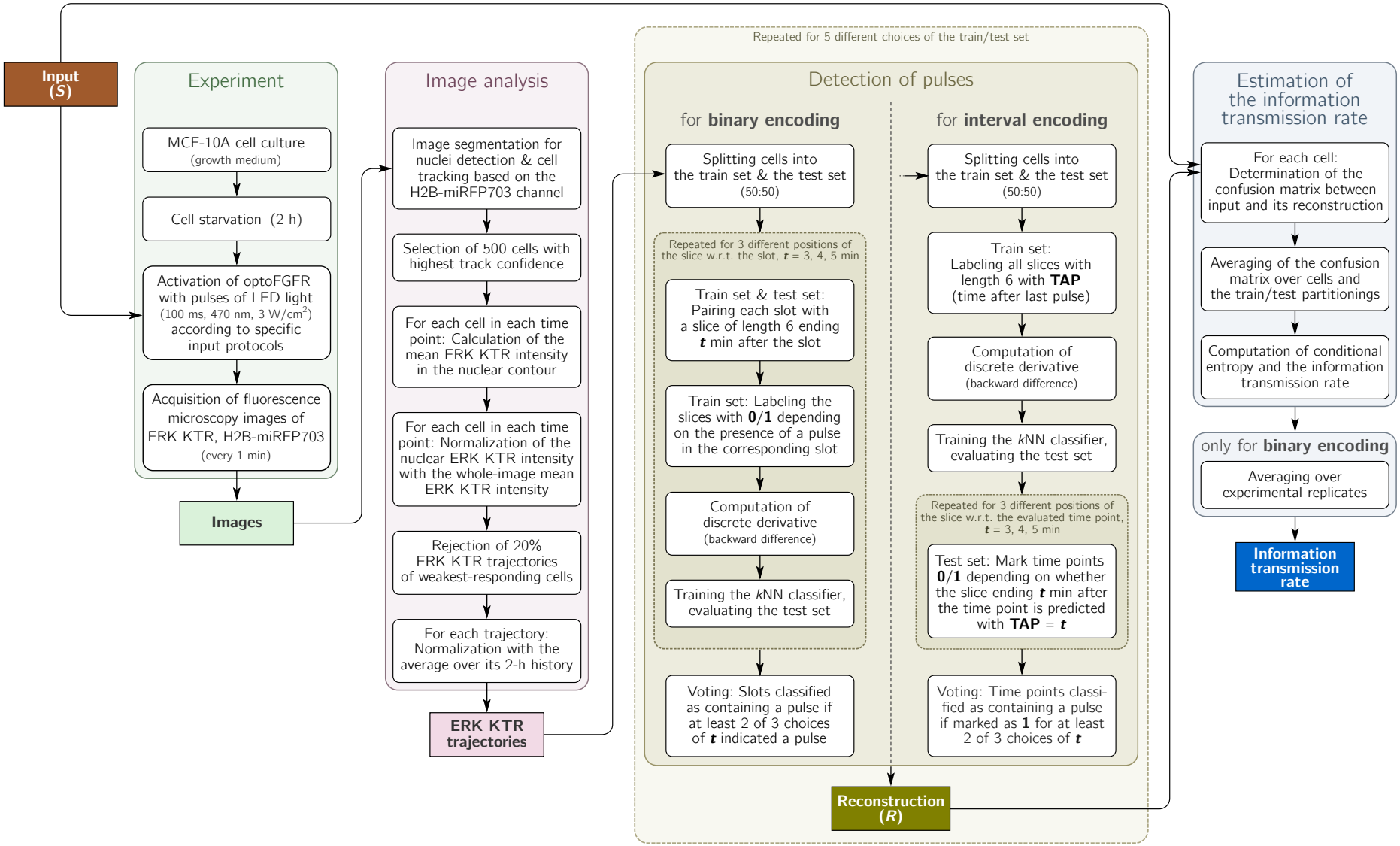

Figure 1—figure supplement 1. Experimental and data analysis workflow.

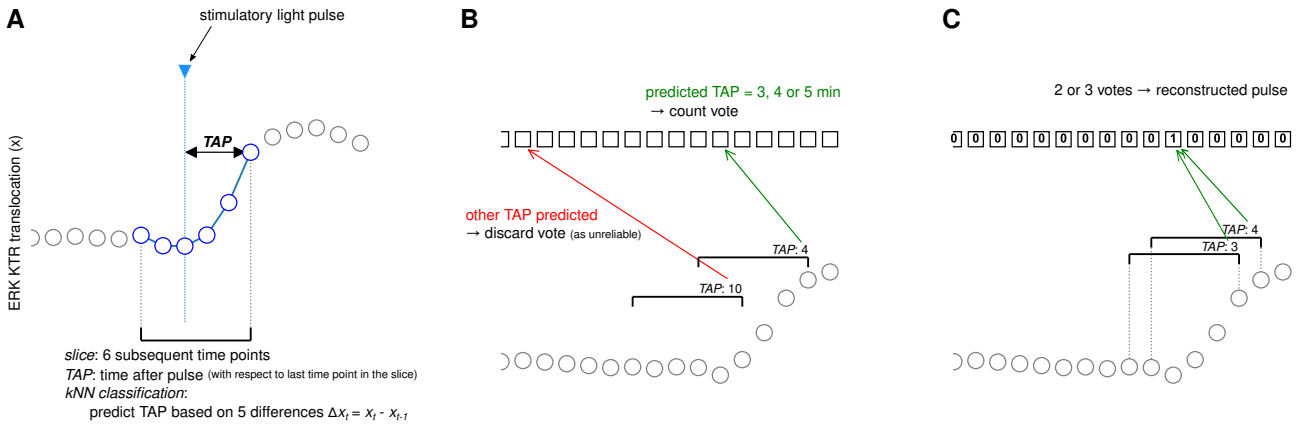

Figure 1—figure supplement 2. Illustration of the input sequence reconstruction algorithm for the interval encoding.

(**A**) Tracks from the training set are segmented into partially overlapping slices of 6 subsequent time points such that each time point belongs to 6 slices. Each slice is labeled with time after pulse (TAP), measured with respect to the last time point in the slice. The *k*NN classifier is trained to predict the TAP associated with each slice.

(**B**) TAP labels of track slices in the test set are predicted with the *k*NN classifier. For each slice, the predicted label indicates the time point at which the stimulation pulse most probably occurred.

(**C**) Votes from different slices are counted. Only votes from slices predicted with TAP = 3,4,5 min are taken into account. Time points that received at least two out of the three possible votes are considered as time points with pulse in the final reconstruction.

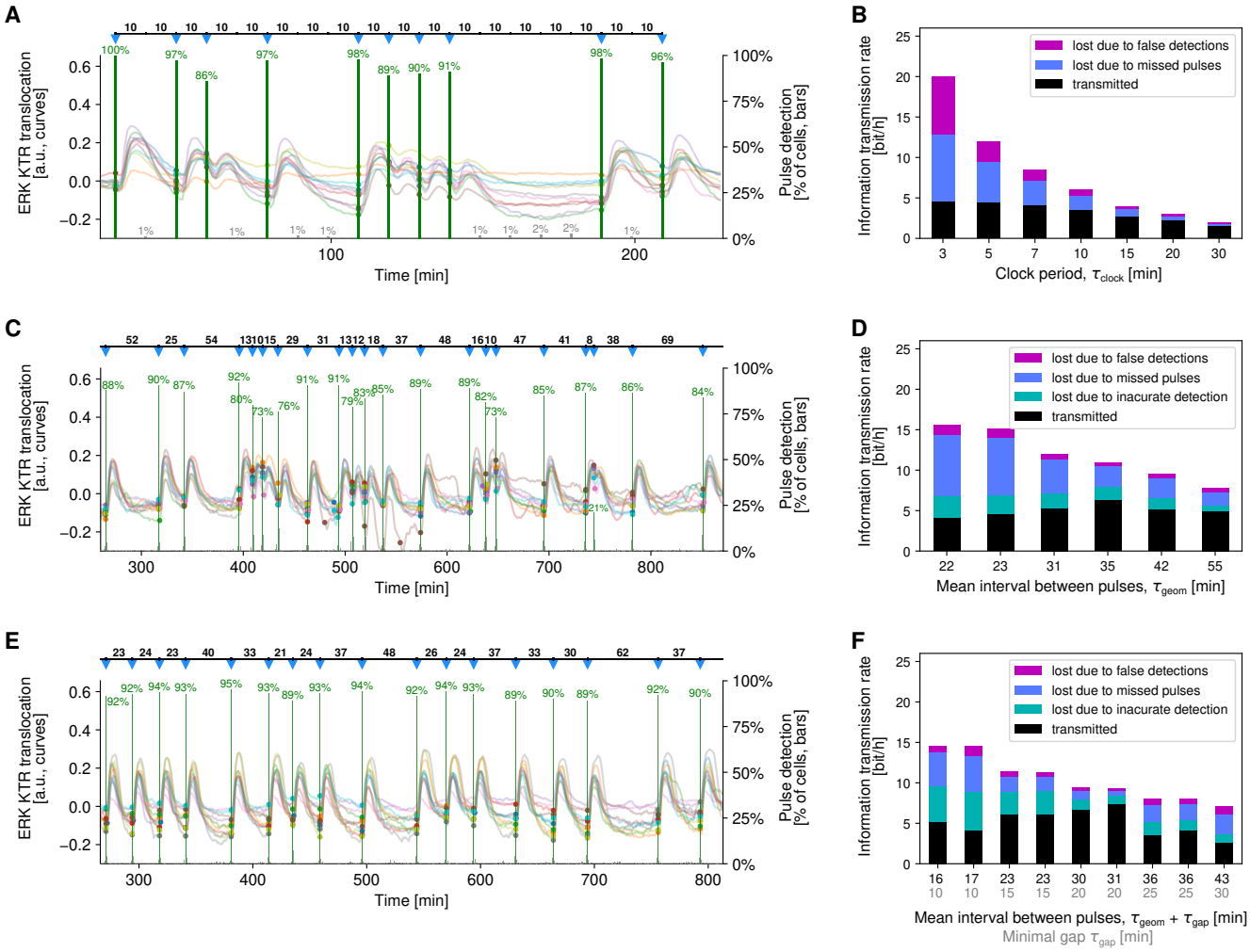

Figure 2. Pulse detection and bitrate estimation in three protocols.

(**A**) Binary encoding: 10 representative trajectories from the experiment with slots every τ_{clock} = 10 min. Stimulation pulses are marked with blue down-pointing triangles. Small filled circles indicate light pulses detected based on the corresponding trajectories. Percentage-labeled green bars in each pulse slot show the fraction of cells in which a pulse was correctly detected. Fractions of false positive detections are shown as percentage-labeled gray bars.

(**B**) Binary encoding: bitrate and sources of bitrate loss in experiments with various clock periods. The number of analyzed cell trajectories was 3200 for clock periods τ_{clock} ranging from 3 to 15 min and 1200 for τ_{clock} = 20 and 30 min. Each analyzed cell trajectory contained 19 clock periods.

(**C**) Interval encoding: 10 representative trajectories from the experiment with the mean interval τ_{geom} = 35 min. Stimulation pulses are marked with blue down-pointing triangles. Colored dots indicate light pulses detected based on the corresponding trajectories. Green bars show the fraction of cells in which a pulse was detected in a particular minute.

(**D**) Interval encoding: bitrate and sources of bitrate loss in experiments with various mean intervals. The number of analyzed cell trajectories was 400 in each of 6 experiments. The number of light pulses in analyzed trajectories was in the range 24–60 depending on the mean interval (all experiments lasted 27–33 h).

(**E**) Interval encoding with a minimal gap: 10 representative trajectories from the experiment with a minimal gap of τ_{gap} = 20 min and the inverse of the optimized geometric distribution parameter τ_{geom} = 10 min. Graphical convention as in panel C.

(**F**) Interval encoding with a minimal gap: bitrate and loss sources in experiments with various minimal gaps and mean intervals. The number of analyzed cell trajectories was 400 in each of 9 experiments. The mean number of light pulses in analyzed trajectories was in the range 19–96 depending on the mean interval (all experiments lasted 27–33 h).

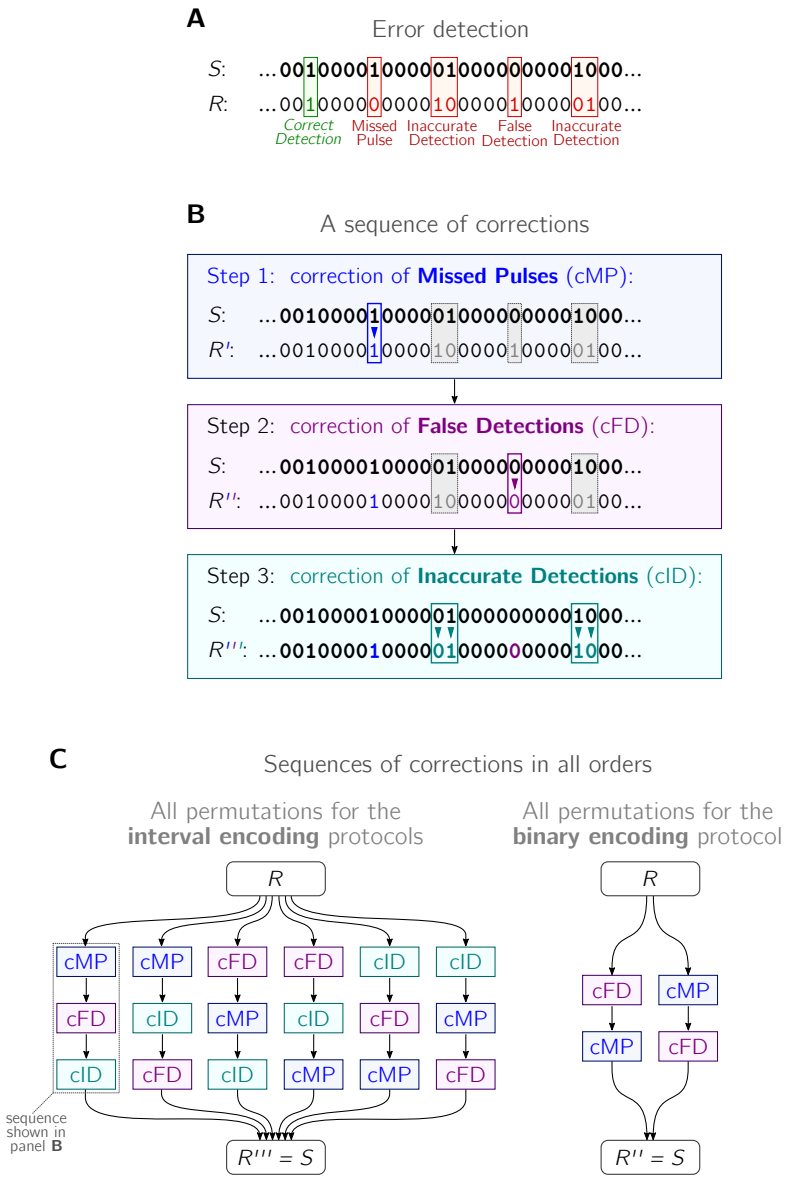

Figure 2—figure supplement 1. The method of estimation of the information transmission rate losses caused by three types of errors.

(**A**) Detection and labeling of errors in the reconstruction *R*. Since patterns of '11' and '101' are guaranteed to never occur in the input sequence *S*, the labeling is non-overlapping and unambiguous. Inaccurate detections in the interval encoding protocols are not decomposed into missed pulses and false detections but subjected to their specific correction type.

(**B**) An example 3-step sequence of error corrections for the interval encoding protocols. After the third step, the fully corrected reconstruction *R*''' is identical to the input sequence *S*.

(**C**) All orders of three-step corrections (for the interval encoding protocols) and two-step corrections (for the binary encoding protocol). Within each encoding protocol, for each type of correction its contribution to reducing the loss of the information transmission rate is estimated for all permutations and then averaged.

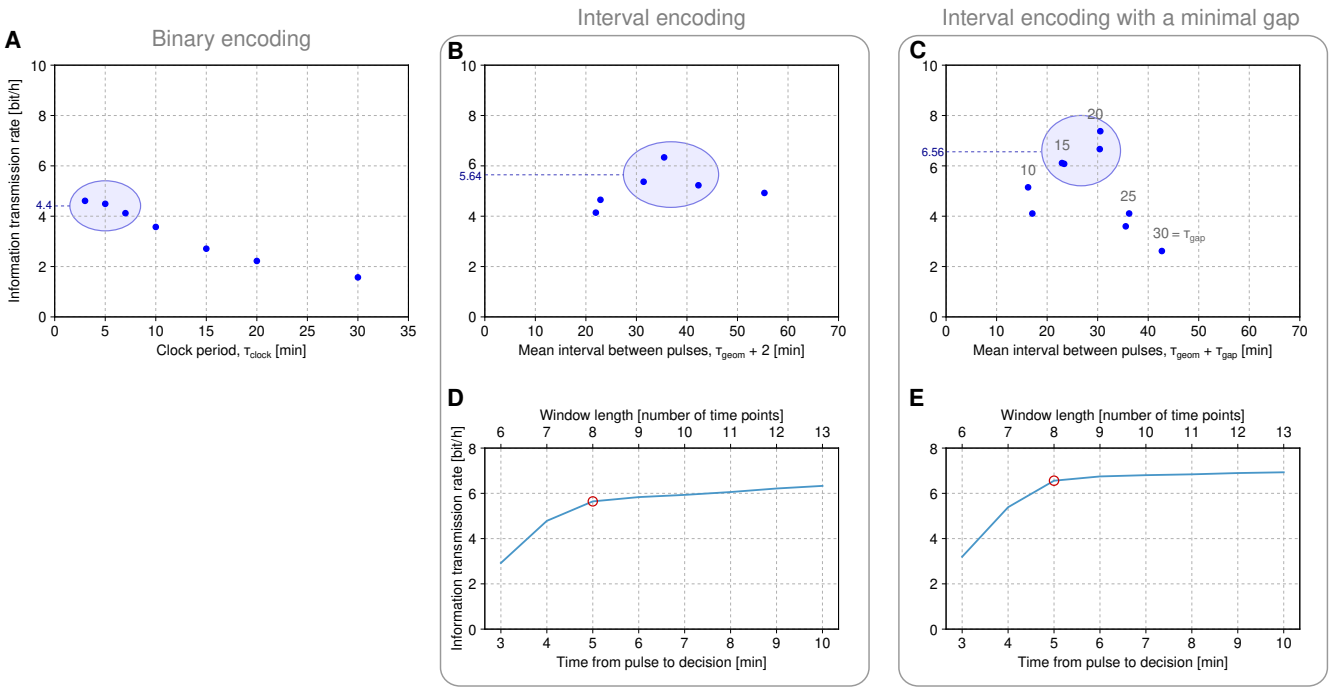

Figure 3. Channel capacity estimation.

(**A**)–(**C**) Information transmission rate for three protocols. The lower bound of channel capacity is estimated as the average of 3 or 4 encircled points and marked with a dashed line.

(**D**)–(**E**) Lower bound of channel capacity as a function of time from pulse to its detection for two interval encoding protocols. Pulse detection is based on the ERK KTR trajectory window that begins 2 min before a pulse slot and ends at the time after the pulse slot indicated on the horizontal axis (classification is always based on three overlapping slices of their length adjusted to the length of the window). The 8 min-long window (red circle) is used for pulse detection throughout the paper.

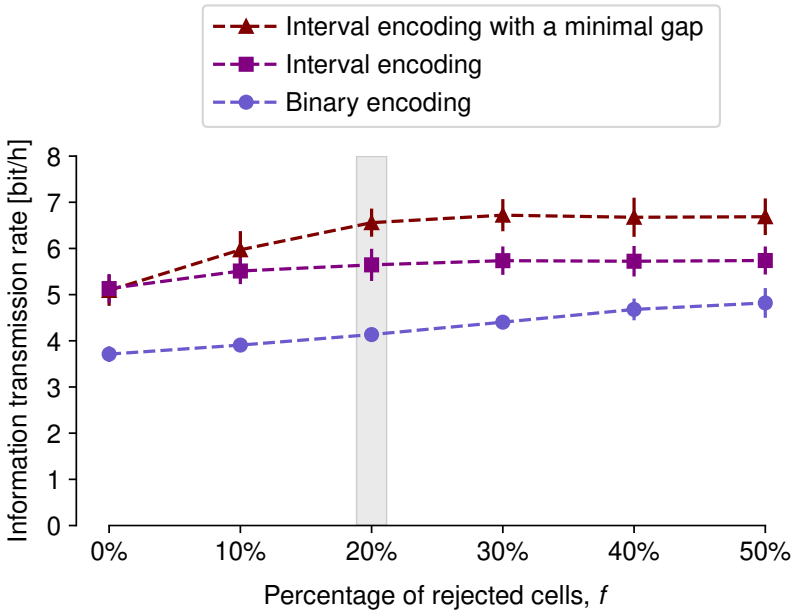

Figure 3—figure supplement 1. Lower bound of channel as a function of the fraction of cells rejected in the preselection step.

The lower bound is computed as in Figure 3. The preselection step is introduced to exclude cells that do not respond to stimulation, possibly due to low expression of optoFGFR or the ERK KTR. The cells are rejected based on a criterion that is a priori independent of the accuracy of pulse detection, see Methods for details. Throughout the paper, the fraction of rejected cells is set to 20% (highlighted in gray), because above this value the bitrate estimates in the interval encoding protocols with and without a gap reach a plateau.

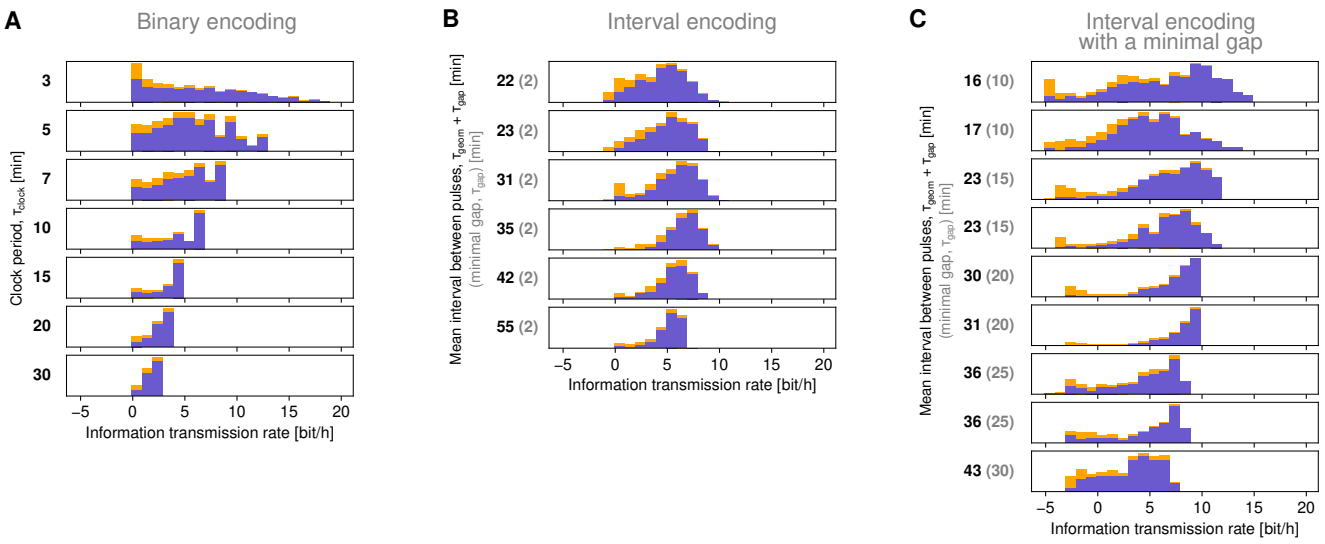

Figure 3—figure supplement 2. Histograms of the information transmission rate in individual cells for (A) binary encoding, (B) interval encoding, and (C) interval encoding with a minimal gap.

Estimates for the cells rejected in the preselection step (20% of all cells) are marked in orange. Negative information transmission rate estimates are possible due to the rough approximation based on inequalities in Eq. (8).